Interplay Between Steric and Electronic Effects: A Joint Spectroscopy and Computational Study of Nonheme Iron(IV)oxo Complexes

DOI:
10.1002/chem.201806430

Document Version
Accepted author manuscript

Interplay Between Steric and Electronic Effects: A Joint Spectroscopy and Computational Study of Nonheme Iron(IV)-oxo Complexes

Gourab Mukherjee,[a] Aligulu Alili,[b] Prasenjit Barman,[a] Devesh Kumar,[c] Chivukula V. Sastri*[a] and Sam P. de Visser*[b]

Abstract: Iron is an essential element in nonheme enzymes that plays a crucial role in many vital oxidative transformations and metabolic reactions in the human body. Many of those reactions are regio- and stereospecific and it is believed that the selectivity is guided by second-coordination sphere effects in the protein. Here, we show results on a few engineered biomimetic ligand frameworks based on the N4Py scaffold (N,N-bis(2-pyridylmethyl)-N-bis(2-pyridyl)methylamine) and study the second-coordination sphere effects. We show here, for the first time, that selective substitutions in the ligand framework can tune the catalytic properties of the iron(IV)-oxo complexes by regulating the steric and electronic factors. In particular, a better positioning of the oxidant and substrate in the rate-determining transition state lowers the reaction barriers. Therefore, an optimum balance between steric and electronic factors mediates the ideal positioning of oxidant and substrate in the rate-determining transition state that affects the reactivity of high-valent reaction intermediates.

Introduction

Metalloenzymes play vital functions for human health and are involved in the biosynthesis of essential compounds in the body as well as the biodegradation of xenobiotics and damaging products.[1,2] Due to the large natural abundance of iron, metalloenzymes with either mononuclear or binuclear iron are relatively common in biology. Studies on the details of enzymatic reaction mechanisms are challenging due to the short lifetime of catalytic cycle intermediates and hence it is not always clear what the active species is that performs the transformations or what features of the active site affect the rate-determining reaction step. In order to understand the functional properties of these metal-containing active sites, biomimetic models have been developed that comprise the metal with a similar coordination environment but dissolved in an organic solvent.[3] Biomimetic models give insight into the effect of the ligands on the chemical properties and reactivity of the oxidant as well as the first and second coordination sphere on the reaction mechanism and rate constants.

Often biomimetic models contain mononuclear iron embedded in a ligand scaffold and pentadentate ligands have proved to be very popular as they generally give few isomeric structures. One particular N5-based pentadentate ligand that has been extensively studied is N4Py: N4Py = N,N-bis(2-pyridylmethyl)-N-bis(2-pyridyl)methylamine, Figure 1.[4] In the iron(IV)-oxo form, the $[Fe^{IV}(O)(N4Py)]^{2+}$ complex (**1b**) has four equatorially bound nitrogen donor atoms (N_{eq}) perpendicular to the iron(IV)-oxo axis and an axial amine nitrogen atom (N_{ax}) *trans* to the oxo group. Structurally, this ligand framework offers a perfect bowl-like cavity for the iron(IV)-oxo for reactions with substrates. In terms of bond-atom distances, all the equatorial Fe–N_{eq} distances appear to be equivalent and give the iron an octahedral symmetry. Over the years, the Fe(IV)-oxo complex (**1b**) has been thoroughly characterized and extensively studied, which therefore is an ideal candidate to engineer with substituents and ligands and study the interplay between the steric and electronic effects on its properties and reactivity.

There have been quite a few reports on the derivatization of pyridine rings that are bound to the iron(IV)-oxo core in **1b**,[5,6] particularly at the pyridine 6-position, which is closest to the oxo group. However, most studies on modified N4Py structures have focused on the two pyridine rings that are tethered to the axial nitrogen atom (N_{ax} atom) through methylene carbon atoms. We, therefore, were wondering what the effect would be of *ortho*-substitution of the two pyridine rings that bind *via* a methine carbon to the axial N-atom. Our study reveals the inequivalence of the four bound pyridine rings, which otherwise appear similar in terms of equatorial ligand field perturbation, when the pyridine C6 positions are substituted and results in dramatic changes in reactivity.

It has been shown that substitution of the 6th position of a pyridine ring leads to the weakening of the equatorial field resulting in elongation of the Fe–N_{eq} bonds due to enhanced electrophilicity of the iron(IV)-oxo species.[6] Thus, using the tetradentate TPA ligand system (TPA = tris-(2-pyridylmethyl)amine) Que and co-workers showed that introduction of at least one methyl group in the ligand framework (in the form of 6-MeTPA, 6-Me_2TPA and 6-Me_3TPA) led to changes in the electronic ground state of the ferrous and ferric species from S = 1 to S = 2.[7]

[a] Mr. G. Mukherjee, Dr. P. Barman, Dr. Chivukula V. Sastri
Department of Chemistry
Indian Institute of Technology Guwahati
Guwahati-781039, Assam, India
E-mail: sastricv@iitg.ac.in
[b] Mr. A. Alili, Dr. S. P. de Visser
The Manchester Institute of Biotechnology and School of Chemical Engineering and Analytical Science, The University of Manchester
131 Princess Street, Manchester M1 7DN, United Kingdom
E-mail: sam.devisser@manchester.ac.uk
[c] Dr. D. Kumar
Department of Applied Physics, Babasaheb Bhimrao Ambedkar University, School for Physical Sciences
Vidya Vihar, Rae Bareilly Road, Lucknow-226025, UP, India
E-mail: dkclcre@yahoo.com
Supporting Information (SI) available: Supporting Information with detailed methodology, experimental characterization of the complexes and reactivity studies performed as well as computational raw data (absolute and relative energies, group spin densities, group charges and Cartesian coordinates) is available. CCDC number 1876766 contains the crystallographic data for this paper that can be obtained free of charge from The Cambridge Crystallographic Data Centre via www.ccdc.cam.ac.uk/structures.

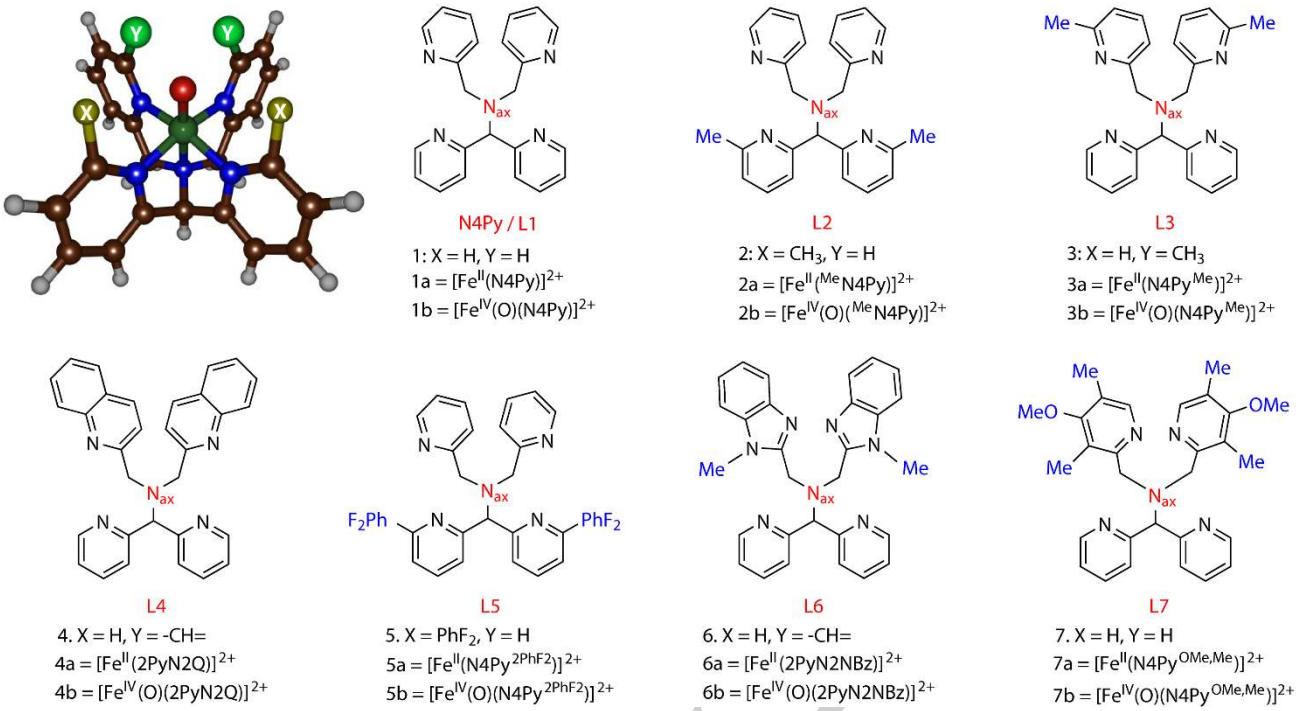

Figure 1. Structures of oxidants discussed in this work.

Introduction of bulkier quinoline groups instead of pyridine led to the formation of a highly reactive high spin ferryl-oxo intermediate with spectroscopic features analogous to the active species of the enzyme taurine/α-ketoglutarate dioxygenase (TauD).[8] Furthermore, drastic improvement in catalytic reactivity has been successfully achieved by replacement of pyridine groups in TPA by bulkier heterocycles such as N-methylbenzimidazole.[9] There are also reports of other (S = 2) iron(IV)-oxo intermediates where the metal center is positioned in a sterically encumbered cavity with forceful occupation of a trigonal bipyramidal geometry.[10]

On account of steric bulk and better σ-donor ability, these engineered ligand frameworks can offer enhanced perturbations in the equatorial ligand field that can make the iron(IV)-oxo core more susceptible to approaching substrates. Steric and electronic effects are two vital tuning probes that manifests the reactivity profiles for these systems and a delicate borderline exists between the two factors.[11] It is understood that along with the stretched Fe–N_{eq} bonds, the distortion in the ferryl axis, specifically the N_{ax}–Fe–O bond angle, plays a pivotal role in their stabilities, spectroscopic properties and various oxidative reactivities.[6] These examples from the literature implicate that substitution of the 6th-position of a metal-bound pyridine ring leads to better hydrogen atom abstraction (HAA) and oxygen atom transfer (OAT) reactivity. However, what most of these metal complexes have in common is that the manipulations have been done in the 6th position of two specific methylene bound pyridine rings in N4Py, while any sort of engineering on the other two methine carbon bound pyridine rings in the primary coordination sphere has rarely been reported. Hence, an effort is made by our groups to dig deeper into this factor. Both experimental and theoretical studies reveal the intrinsic parity between the two sets of pyridine rings, contributing to the overall reactivity profiles of the two catalysts. Considering the frameworks shown in Figure 1, the ligands are named 2(6-MePy)N_{ax}2Py or ^{Me}N4Py and 2PyN_{ax}2(6-MePy) or N4Py^{Me} in short and their iron(II) complexes are designated **2a** and **3a**, respectively.

The distinct spectroscopic properties and stability of the two complexes $[Fe^{IV}(O)(^{Me}N4Py)]^{2+}$ (**2b**) and $[Fe^{IV}(O)(N4Py^{Me})]^{2+}$ (**3b**) allowed us to pursue a detailed kinetic analysis and probe into the very definitive factors that govern the reactivity and stability of these high valent metal-oxo species. Our studies concern the fine line between steric and electronic factors that orchestrate the reaction rates and selectivity and also reveal the intricate details of second coordination sphere effects related to substrate approach to a metal-oxo species.

Table 1. Selected bond lengths (Å) and bond angles (°) for Fe(II) complexes **1a-7a**.

Complex:	**1a** [a]		**2a** [b]		**3a** [c]		**4a** [d]		**5a** [e]		**6a** [f]		**7a** [g]	
Bond	*Bond length*	*Avg*	*Bond length*	*Avg*	*Bond length*	*Avg*	*Bond length*	*Avg*	*Bond length*	*Avg*	*Bond length*	*Avg*	*Bond length*	*Avg*
Fe1-N1	1.976 (3)	1.971 [h]	2.049 (5)	2.012 [h]	2.004 (4)	2.036 [h]	2.199 (6)	2.220 [h]	2.057 (1)	2.008 [h]	1.964 (3)	1.977 [h]	1.963 (8)	1.971 [h]
Fe1-N3	1.967 (3)		2.043 (6)		1.981 (4)		2.233 (8)		2.031 (1)		1.983 (3)		1.971 (8)	
Fe1-N4	1.975 (3)		1.974 (5)		2.083 (4)		2.223 (6)		1.979 (1)		1.983 (3)		1.965 (7)	
Fe1-N5	1.968 (3)		1.981 (5)		2.078 (3)		2.226 (6)		1.966 (1)		1.979 (2)		1.984 (8)	
Fe1-N_{ax}	1.961 (3)	1.938 [i]	1.968 (5)	1.949 [i]	1.990 (2)	1.974 [i]	2.192 (6)	2.118 [i]	1.967 (1)	1.949 [i]	1.983 (3)	1.942 [i]	1.959 (7)	1.938 [i]
Fe1-N6	1.915 (3)		1.930 (5)		1.959 (3)		2.045 (6)		1.930 (6)		1.901 (3)		1.918 (7)	
Avg Fe-N	1.960		1.991		2.016		2.186		1.988		1.965		1.960	
Angles	*Bond angles*		*Bond angles*		*Bond angles*		*Bond angles*		*Bond angles*		*Bond angles*		*Bond angles*	
∠ N_{eq}-Fe-N_{ax} [j]	84.0		83.3		82.7		77.2		83.5		83.6		84.0	
∠ N_{eq}-Fe-N6 [j]	96.0		96.6		97.1		102.6		96.6		96.4		96.0	
∠ N_{ax}-Fe-N6	177.3		179.3		167.5		168.3		175.5		175.7		176.9	

[a] Ref [13a], [b] This work, [c] Ref [13b], [d] Ref [6c], [e] Ref [5d], [f] Ref [5f], [g] Ref [5g], [h] Average of all the equatorial bonds, [i] Average of all the axial bonds, [j] Average *cis*-bond angle of equatorial Fe1–N bonds with N_{ax} and N6. "*Avg*" stands for average.

Results

Experimental Characterization

Ligands ^{Me}N4Py and N4Py^{Me} were synthesized starting from di(6-methyl-pyridin-2-yl)methanone or di(pyridine-2-yl)methanone and in a reaction with hydroxylamine converted into an oxime and subsequently over Zn reduced further to their amine form. Upon addition of either 2-(chloromethyl)-pyridine or 2-(chloromethyl)-6-methyl-pyridine in NaOH we reacted the amines to form the ^{Me}N4Py and N4Py^{Me} structures, respectively, in good yield (detailed synthetic procedures are discussed in the Supporting Information, Scheme S1 and S2). Subsequently, the ^{Me}N4Py and N4Py^{Me} ligands were reacted with $[Fe^{II}(CH_3CN)_2 \cdot 2ClO_4]$ in acetonitrile to form the metal complexes $[Fe^{II}(^{Me}N4Py)](ClO_4)_2$ (**2a**) and $[Fe^{II}(N4Py^{Me})](ClO_4)_2$ (**3a**), which were characterized with UV-vis absorption spectroscopy, electrospray ionization-mass spectrometry (ESI-MS), and crystallographic methods.[12] Single crystals of **2a** were obtained by vapor diffusion of diethyl ether in an acetonitrile solution of $[Fe^{II}(^{Me}N4Py)(CH_3CN)]^{2+} \cdot 2BF_4$.

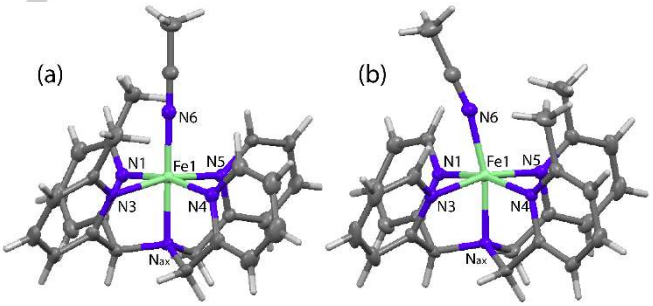

Figure 2. ORTEP diagram (with 30% ellipsoid probability) of complex (a) $Fe^{II}(^{Me}N4Py)(CH_3CN)](BF_4)_2$ and (b) $Fe^{II}(N4Py^{Me})(CH_3CN)](ClO_4)_2$. [13b] Color-coding: Hydrogen (off-white), carbon (gray), iron (green), nitrogen (violet). Counter-ions have been omitted for clarity.

The crystal structure (Figure 2a and Table 1) shows clear 5-coordination of the metal to the ^{Me}N4Py ligand in a structural orientation analogous to the reported complexes, $[Fe^{II}(N4Py)]^{2+}$ and $[Fe^{II}(N4Py^{Me})(CH_3CN)]^{2+} \cdot 2ClO_4$.[13] The Fe–N bond distances for **2a** as shown in Table 1 and are typical for low spin Fe(II) complexes reported previously.[5,6,11,13] In comparison to the crystal structure of Feringa and co-workers,[13b] (Figure 2b, Table 1) the two metal complexes **2a** and **3a** indicate minor differences.

In particular, the sixth coordination position, *trans* to the N_{ax}, is occupied by the solvent CH_3CN in both the complexes, but there is a substantial bending in the N_{ax}–Fe-solvent axis for **3a** (167.5°), as compared to **2a** (179.3°). This is the maximum bend observed among the fellow structures (Table 1) and is close to that in **4a** reported by Rana *et al* where a triflate counter-anion occupies the apical position instead of a solvent molecule.[6c] The huge tilt accounts for an induced steric effect imparted by the methyl groups in the structure of **3a**. Another interesting observation is that in **2a,** the N_{ax}–Fe–solvent axis is closest to 180° in agreement with **1a** (177.3°). Thus, in the absence of any substituent the bond angle deviates from 180° to an acute value (177.3° in **1a**), and substituents in the methylene bound pyridine rings (167.5 in **3a**, 168.3 in **4a**, 175.7 in **6a** and 176.9 in **7a**) and even methine bound pyridine rings (as in **5a**) display the same tilt. By contrast, in **2a** the steric effect acts from the opposite direction thereby making the axis almost as straight as 180°. The $\angle N_{eq}$–Fe–N_{ax} and $\angle N_{eq}$–Fe–N_6 angles (compiled in Table 1) give a measure of the position of Fe in the equatorial plane inside the ligand framework and signifies the depth, to which the metal center is located inside the cavity. Again, complex **4a** and then **3a** have the lowest $\angle N_{eq}$–Fe–N_{ax} and highest $\angle N_{eq}$–Fe–N_6 values compared to the rest indicative of the strain inside the cavity (although there are intrinsic differences in ligation ability for the 6th donor which is N for **3a** and O for **4a**).

Furthermore, the average Fe–N bond distance is higher in **3a** (2.016 Å) than that in **1a** (1.960 Å), **2a** (1.991 Å), **5a** (1.988 Å), **6a** (1.965 Å) and **7a** (1.96 Å). This is imperative of a weakened equatorial ligand field in complex **3a.** Considering the cavity provided by the N5 donor center in all the ligand systems, the 6th coordination site is occupied by the solvent molecule that is susceptible to be replaced by the oxygen atom during the formation of the oxo species. Indeed, the fragility of the Fe-solvent bond is indicated by the Fe1–N6 bond length which is also longer in **3a** (1.959(3) Å) compared to **1a** (1.915(3) Å), **2a** (1.930(5) Å), **5a** (1.930(6) Å), **6a** (1.901(3) Å) and **7a** (1.918(7) Å). The Fe–O_{OTf} bond length is 2.045(6) Å in **4a** is even longer than the Fe–N6 bond in **3a**. The higher bond length values in **4a** are most probably due to the high spin nature of the complex as a result of anion binding (triflate) to the 6th coordination site instead of CH_3CN that generally results in low spin complexes. Thus, *albeit* the intrinsic differences between the Fe–N and Fe–O bonds, the quinoline groups impart strong influence on the vertical N_{ax}–Fe–O axis which is obvious from the huge OAT rates.[6b] Clearly, the positioning of the methyl groups is responsible for similar steric effects in **3a** that can be anticipated for the corresponding oxo complex (**3b**) as well.

Unlike in the solid state, structural tuning of the ligand skeleton of such Fe(II) complexes often leads to spin-equilibrium in the solution phase. The absorption spectra of all Fe(II) complexes **1a**, **2a** and **3a**, show two MLCT bands with notable differences in their epsilon values ($^{1a}\varepsilon$ = 8120, 6600 L M^{-1} cm^{-1}, $^{2a}\varepsilon$ = 5360, 4920 L M^{-1} cm^{-1} and $^{3a}\varepsilon$ = 880, 400 L M^{-1} cm^{-1}), see Figure S6a, Supporting Information. The very low epsilon value is speculative of substantial spin crossover in **3a** and **2a** which is absent in **1a**. Steric hindrance of the methyl groups increases the bond lengths in the solid state; however, in the solution state, the spin-equilibrium is mostly shifted towards the high spin form that also rationalizes the low epsilon values of the new complexes. As the temperature is lowered to 233 K, the population of the low spin state increases effectively in **3a** and **2a** thereby increasing their absorbance values (see Figure S6, Supporting Information). The ^{1}H-NMR spectra of **2a** and **3a** further support these findings and expectedly paramagnetic shifting of the peaks were observed in both the cases (see Figure S7, Supporting Information). However, the extent of peak-shifting and broadening is more in case of **3a** than in **2a**, thereby confirming larger contribution of the high spin form in **3a** in equilibrium with the low spin species. Similar paramagnetic shifting of proton resonances for ferrous complexes was also observed for **4a** and **6a**.[5f,6]

Complexes **2b** and **3b** were generated *in situ* by treating the iron(II) precursor complexes with 1.5 equivalents of $PhI(OAc)_2$ in an acetonitrile solution at room temperature. These ferryl-oxo complexes were characterized by UV-vis, ESI-MS and ^{1}H-NMR spectroscopy. Upon addition of oxidant to the Fe(II) species, the Fe^{IV}=O chromophores were formed almost instantaneously for both **2b** and **3b** as observed from the UV-vis spectrum. Subtle differences in the absorption spectrum were seen for the iron(IV)-oxo complexes **1b**, **2b** and **3b** (Figure 3). Cumulative bathochromic and hypochromic shifts range from 695 nm (ε = 400 L M^{-1} cm^{-1}) for **1b** to 750 nm (ε = 340 L M^{-1} cm^{-1}) for **2b** to 775 nm (ε = 200 L M^{-1} cm^{-1}) for **3b**. These changes in the d-d transition bands are indicative of the sequential increment of the equatorial ligand field perturbation along the series and weakening of the same. Furthermore, this also leads to distortions in the bell shaped absorption curve of **2b** and **3b** due to the appearance of shoulder humps in the NIR region as compared to that of **1b**. The stability of these complexes also follows the same trend with half-lives of 3600, 130 and 30 minutes, respectively.

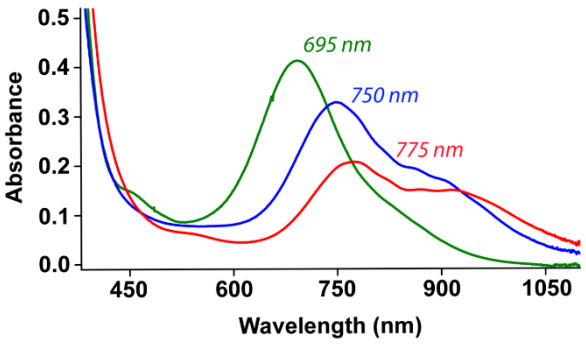

Figure 3. UV-vis absorption spectrum of **1b** (*green*), **2b** (*blue*) and **3b** (*red*) in CH_3CN at 298 K

The relatively less stable nature of the new oxo complexes (as evident from their half-lives) made it difficult to record their ESI-MS spectra at room temperature. Therefore, the ESI-MS spectra for **2b** and **3b** were recorded at lower temperatures by infusing cold samples directly into the source. Both complexes gave a major peak at *m/z* 233.6 corresponding to $[Fe^{IV}(O)(L)]^{2+}$ (Figure S8, Supporting Information). To further confirm the existence of iron(IV)-oxo, we did an isotope labelling experiment. The iron-oxo complexes are known to exchange oxygen from water.[14] Thus upon addition of $H_2{}^{18}O$ to the new iron-oxo complexes, a positive peak shift of one unit for the M/2 ion-cluster was observed in the mass spectrum after an incubation spell of 10 – 15 minutes thereby confirming the existence of iron(IV)-oxo complexes (see insets in Figures S8).

We also carried out ^{1}H-NMR spectroscopy experiments to discriminate between the two new iron(IV)-oxo species, **2b** and **3b**, (Figure 4) and compare the spectra with the existing ^{1}H-NMR spectrum of complex **1b**.[15] Clearly, there are shifting of peaks resulting from the typical S = 1 ferryl species that unequivocally exists in the octahedral environment.[15] The low spin Fe(IV) center in **2b** enjoys more favorable relaxation properties compared to **3b** thereby producing sharper signals although both the complexes give rise to paramagnetically shifted proton resonances. As compared to the ^{1}H-NMR spectra of **4b**, the same for **2b** and **3b** appears less complex due to the absence of the quinoline ring protons.[6b,c] The ^{1}H-NMR spectra for **2b** and **3b** were recorded over a spectral width of 200 ppm at 298 K temperature (Figure 4). Both complexes show a unique shift pattern for the pyridine protons of low spin Fe(IV) centers, with one β-proton shifted upfield (-17.2, -8.6 ppm for **2b** and -12.4, -8 ppm for **3b**) and one β-proton shifted downfield (43.6, 47.8 ppm for **2b** and 32.8, 43.9 ppm for **3b**) as observed previously for analogous complexes.[5b-5e,15] However, in case of Fe(III)-pyridine complexes, both the β-protons shift downfield with comparable paramagnetic shift.[7] The different amount of paramagnetic shifts and peak integrations in the NMR spectra of **2b** and **3b** justify the unequal interaction of the two different sets of pyridine rings with the Fe d-orbitals that have uneven load of unpaired spin density.

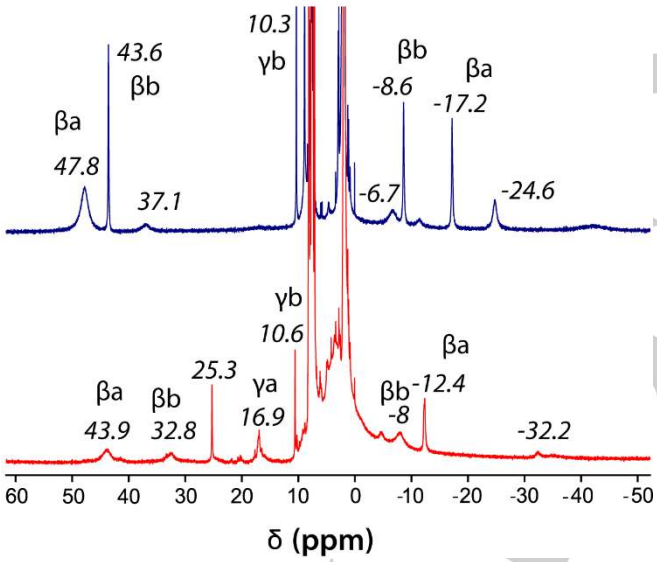

Figure 4. ^{1}H-NMR spectra of **2b** (*top*) and **3b** (*bottom*) in CD_3CN at 298 K.

Reaction Kinetics

The reactivity of these complexes was investigated for the oxygen atom transfer (OAT) and hydrogen atom abstraction (HAA) reactions from substrates. Thioanisole was employed initially for OAT reactivity while HAA properties were tested using a range of substrates having varied C–H bond dissociation energies and active hydrogen availability. Addition of substrates to a solution containing **2b** or **3b** in acetonitrile led to the first-order decay of the characteristic *d-d* transition band in the respective UV-vis spectrum. The second-order rate constants (k_2) were determined by plotting the pseudo first-order rate constants (k_{obs}) as a function of the proportional increment of substrate concentration. In the case of OAT, the sulfur atom of the organic substrate acts as the active recipient of the oxygen atom and eventually forms the oxidized product in the form of sulfoxides or sulfones.[16–18] $[Fe^{IV}(O)(N4Py)]^{2+}$ (**1b**) reacts with thioanisole with a k_2 of 50 × 10^{-3} M^{-1} s^{-1} at 273 K.[17]

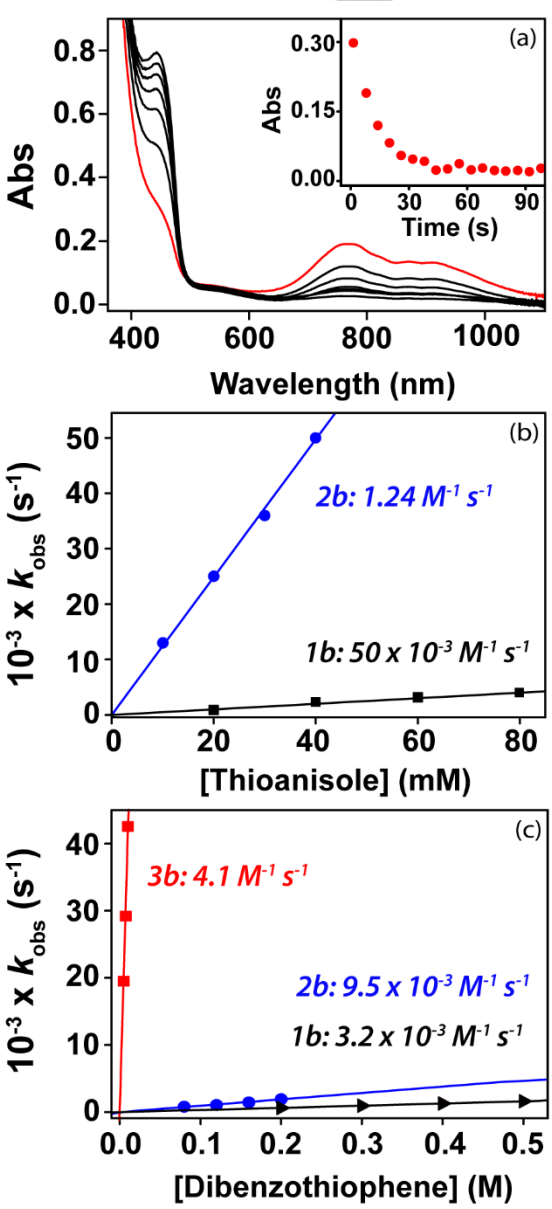

Figure 5. (a) Decay profile for the reaction of **3b** with THA (5 equivalents) at 233 K. Inset shows the time trace for the decay of the 775 nm band. Second-order rate constants determined for the reaction of **1b** (1 mM, ►), **2b** (1mM, ●) and **3b** (1 mM, ■) with (b) thioanisole at 273 K; (c) DBT at 298 K.

Under identical conditions, complex **2b** shows enhanced reaction rates (see Figure 5b). However, upon addition 10 equivalents of thioanisole to 1 mM solution of **3b**, the 775 nm band vanished in less than 20 seconds at even lower temperatures (233 K). As such, complex **3b** reacts with thioanisole at even faster rates than recently reported $[Fe^{IV}(O)(2PyN2Q)]^{2+}$ complex (**4b**) under identical conditions: for 5 equivalents THA at 233 K, $^{3b}k_{obs}$ = 8.9(4) × 10^{-2} s^{-1} and $^{4b}k_{obs}$ = 5.4(2) × 10^{-2} s^{-1}.[6b] Therefore, in order to procure a comparative

analysis for S-oxidation under identical conditions, we employed dibenzothiophene (DBT) as the model substrate for OAT reactions for all three oxidants. DBT has two benzene rings fused to a thiophene, in conjugation with the heteroatom, and delocalizes the electron density through a number of canonical structures thereby making the reaction slower compared to thioanisole.[18] Thus, it is a more suitable substrate for a comparative study of all three complexes than thioanisole. Complex **3b** transfers an oxygen atom to DBT about a thousand times faster (k_2 = 4.1 M^{-1} s^{-1}) than **1b** (k_2 = 3.2 × 10^{-3} M^{-1} s^{-1})[18] whereas **2b** (k_2 = 9.5 × 10^{-3} M^{-1} s^{-1}) could only triple **1b** (see Figure 5c) at 298 K. These rates second the fact that complex **3b**, compared to **2b**, has an underlying weaker equatorial Fe–N bonding and more ferryl-oxo distortions thereby making the catalyst more susceptible towards heteroatom oxidation reactions. Hence, introduction of methyl groups at the two methylene bound pyridine rings exerts a prolific effect on the iron-oxo core compared to the one containing methyl groups on the pyridine rings connected by the methine carbon in the case of OAT reactions.

To verify the sustainability of this reactivity trend for HAA, we evaluated the C–H activation abilities of the complexes under study. The conversion of ethylbenzene to 1-phenylethanol was tested with **1b**, **2b** and **3b**. Reaction rates with **3b** (k_2 = 155.3 × 10^{-3} M^{-1} s^{-1}) was around twenty times faster than **1b** (k_2 = 8 × 10^{-3} M^{-1} s^{-1}); whereas **2b** (k_2 = 9.7 × 10^{-3} M^{-1} s^{-1}) almost mirrors **1b** in terms of C–H activation rates at 298 K (see Figure 6a). To ensure that HAA is the rate-determining step, we repeated the experiment with ethylbenzene-[D_{10}] (see Figure S12, Table S8, Supporting Information).[4b] The isotopomers react differently due to vibrational differences in the C–H and C–D bond frequencies and kinetic isotope effect (KIE) values of 14 and 13 were obtained for **2b** and **3b** respectively. Hence, C–H bond cleavage is the rate-determining step in the HAA reactions.

A more pragmatic approach was made to study the effect of the methyl groups towards substrate approach and reactivity using the conventionally available substrates with varying C–H bond dissociation energies (BDE).[4b,17a] As can be seen in the Bell-Evans-Polanyi plot, the log k_2' values for five different complexes (**1b**, **2b**, **3b**, **4b** and **6b**) is portrayed against the C–H BDE of the sacrificial C–H bond(s) ranging from 77 to 90 kcal mol^{-1} (see Table S9, Supporting Information). As evident from Figure 6b, **1b** and **2b** display almost the same reaction rates for all the substrates. The only exceptions being 9,10-dihydroanthracene (DHA), fluorene and triphenylmethane, where **2b** happens to react very sluggishly compared to **1b**. Clearly the steric effect imparted by the methyl groups in **2b** during the approach of these three bulky substrates can be perceived. Other complexes *viz.* **3b**, **4b** and **6b** have substantially higher reaction rates than **1b**/**2b** for all the substrates irrespective of the C–H bond strength, one specific case, again, being the reactivity of **3b** with triphenylmethane where a significant drop in reaction rate is observed. All the points in the plot shown here have been recorded under similar reaction conditions. Therefore, the sudden drop in reactivity for **2b** and **3b** with triphenylmethane can only be attributed to the steric factor between the oxo complex and the approaching substrate. The only active hydrogen atom in Ph_3CH is deeply embedded inside its '*propeller shaped*' structure, abstraction of which by **2b** and/or **3b** is highly hindered by the steric fencing provided by the methyl groups in both the complexes. This observation is unique and novel and portrays the steric effect of Fe(IV)-oxo complexes with bulky substrates like Ph_3CH (also 9,10-DHA and fluorene) whereas all other complexes (like **1b**, **4b** and **6b**) follow the thermodynamic trend of bond strength *vs* reactivity and the corresponding points for BDE 81 kcal mol^{-1} falls close to the best fitted line. For substrates other than Ph_3CH, the active hydrogen(s) is/are easily accessible to all the complexes depending upon the geometry and approach pathway. Complex **4b** and **6b** have almost similar reactivity profile to **3b** but do not show reluctance towards Ph_3CH, as such, the influence of the added substituents in the pyridine-6 position is primarily electronic thereby enhancing their reactivity compared to **1b**.[5f,6] The longer Fe–N bond length in Fe(IV)-oxo, in general, gives rise to a more reactive complex. The average Fe-N bond lengths in **4b** and **6b** are 2.053 Å and 1.999 Å, while the same for **1b** is 1.972 Å.[6a] Again in complex **2b** and **3b**, the introduction of the methyl groups in the *ortho*-position of the pyridine rings leads to a flagpole-like interaction with the oxo moiety; and the sp^3 hybridization of the methyl carbon thereby adds up to the flexibility in terms of C–C bond rotation and bending. In **4b** and **6b**, however, the added bulk is tethered to the *ortho*- and *meta*-position of the pyridine ring and that to the immediate vicinity of the binding N is an sp^2 carbon thereby restricting its free movement and rotation (see Figure 1).

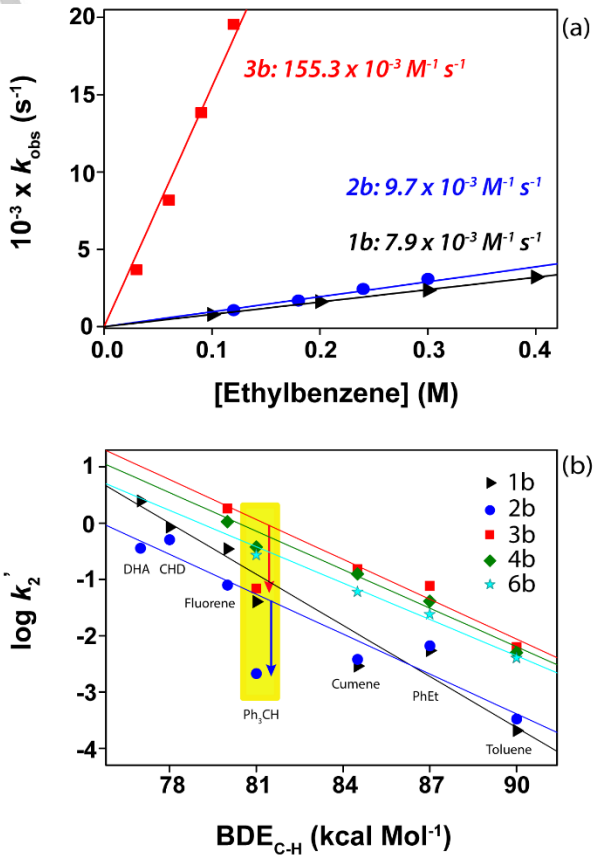

Figure 6. (a) Second-order rate constants determined for the reaction of **1b** (1 mM, ►), **2b** (1mM, ●) and **3b** (1 mM, ■) with ethylbenzene at 298 K; (b) Bell Evans Polanyi plot for their reaction of **1b** (►), **2b** (●) **3b** (■), **4b** (♦) and **6b** (★) with different substrates at 298 K in CH_3CN; k_2' is k_2 divided by the number of equivalent C–H bonds on the substrate that would react with the iron(IV)-oxo species. Best fit lines exclude points for Ph_3CH to show the deviation.

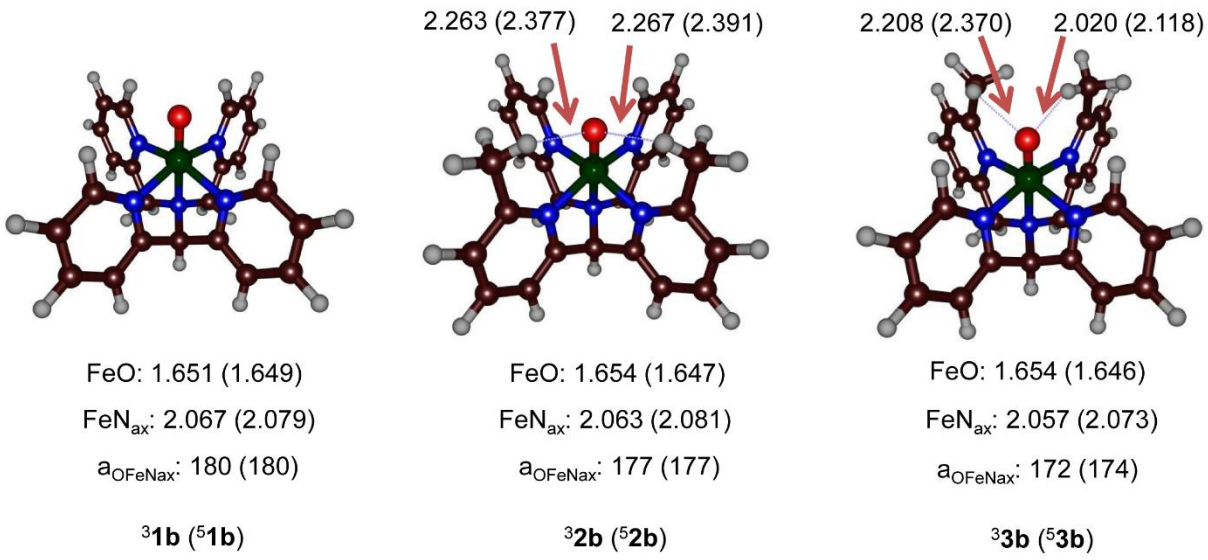

Figure 7. Optimized UB3LYP/BS1 geometries of ^{3,5}**1b**, ^{3,5}**2b** and ^{3,5}**3b** with bond lengths in angstroms and the O–Fe–N$_{ax}$ angle in degrees with N$_{ax}$ the axial amine nitrogen atom.

Overall, in **2b** and **3b**, the steric factor precedes the electronic factor to determine the fate and rate of a reaction, and triphenylmethane (in spite of having a lower BDE$_{C\text{-}H}$) is an ideal substrate to judge the same.

Computational studies

To understand the anomaly in reactivity of **1b** versus **2b** and **3b**, a theoretical investigation was conducted. Before going into the details of the various reaction mechanisms we will discuss the electronic and structural differences of the oxidants first.

Figure 7 displays optimized geometries of complexes **1b**, **2b** and **3b** in the lowest triplet and quintet spin states. In all cases the triplet spin state is the ground state and well separated from the nearest quintet spin state. In particular, triplet-quintet energy gaps of 4.0 and 2.3 kcal mol^{-1} are found for **2b** and **3b**, respectively. For structure **3b** we also calculated the lowest lying singlet and septet spin states, which we find 28.9 and 20.6 kcal mol^{-1} higher in energy, respectively. As such, these spin state surfaces were not explored further. Our spin-state energies and spin-state orderings match previously calculated DFT studies on [Fe^{IV}(O)(N4Py)]$^{2+}$ (**1b**) excellently, where triplet-quintet energy gaps of well over 4 kcal mol^{-1} were calculated.[17] Moreover, experimental EPR and Mössbauer studies identified **1b** as a triplet spin iron(IV)-oxo species.[4] Therefore, methyl substituents have a small effect on the spin-state energies of **1b**, **2b** and **3b** but do not change the spin-state ordering.

The Fe–O distances are short and typical for a double bond between the iron and oxo group. Although the Fe–O distances in ^{3}**2b** and ^{3}**3b** are the same (1.654 Å), the Fe–O stretch vibration changes from 856 cm^{-1} for the former to 848 cm^{-1} for ^{3}**3b**. These distances match previously reported bond lengths and vibrations of calculated geometries as well as experimental crystal structure distances of iron(IV)-oxo complexes well.[19,20] No dramatic changes in iron(IV)-oxo distances are seen upon addition of methyl substituents to the pyridine scaffold. Similarly, the distances of the iron atom to the axial amine nitrogen atom (N$_{ax}$) do not vary a lot between the individual complexes. The only structural change that is seen comes from a modest bent O–Fe–N$_{ax}$ angle in ^{3,5}**3b** to 172° (triplet) and 174° (quintet), respectively that was envisaged from the crystal structures for the ferrous complexes. This bending may affect the orbital shapes and energies. Note also the weak interactions of the methyl protons to the oxo group at a distance of 2.0 – 2.4 Å in the ^{3,5}**2b** and ^{3,5}**3b** structures. The electronic configuration of the iron(IV)-oxo complexes is determined by the interaction of the metal 3d orbitals with first-coordination sphere ligands and particularly the oxo group. With the molecular *z*-axis associated along the Fe–O bond this gives a pair of bonding and antibonding orbitals for the π and π^* interaction of 3d(Fe) with 2p(O) with a total for six electrons: $\pi_{xz}^2\ \pi_{yz}^2\ \pi^*_{xz}{}^1\ \pi^*_{yz}{}^1$. A final π-type orbital is located in the *xy*-plane and is non-bonding (π^*_{xy}). Two σ-type orbitals associated with the bonding and antibonding interactions along the Fe–O axis (σ_{z2} and σ^*_{z2}) and in the *xy*-plane with pyridine nitrogen atoms ($\sigma_{x2\text{-}y2}$ and $\sigma^*_{x2\text{-}y2}$). Figure 8 gives orbital depictions of ^{3}**2b** as calculated in Gaussian for the α- and β-set of molecular orbitals. The σ_{z2} and $\sigma_{x2\text{-}y2}$ orbitals are low in energy and not shown. In general, all triplet spin states have orbital occupation $\sigma_{z2}^2\ \sigma_{x2\text{-}y2}^2\ \pi_{xz}^2\ \pi_{yz}^2\ \pi^*_{xy}{}^2\ \pi^*_{xz}{}^1\ \pi^*_{yz}{}^1$, whereas the quintet spin state had $\sigma_{z2}^2\ \sigma_{x2\text{-}y2}^2\ \pi_{xz}^2\ \pi_{yz}^2\ \pi^*_{xy}{}^1\ \pi^*_{xz}{}^1\ \pi^*_{yz}{}^1\ \sigma^*_{x2\text{-}y2}{}^1$ configuration. Therefore, a triplet to quintet transition results from the promotion of one electron from π^*_{xy} into $\sigma^*_{x2\text{-}y2}$. A comparison of the orbital shapes of ^{3}**2b** (Figure 8) and ^{3}**3b** (Figure S14, Supporting Information) shows very little differences in orbital shapes. Relative orbital energies as taken from the UB3LYP/BS2 and UB3LYP/BS1 calculations are given in Figure 8. Little variation between the data is seen and most numbers are within a few kcal mol^{-1}.

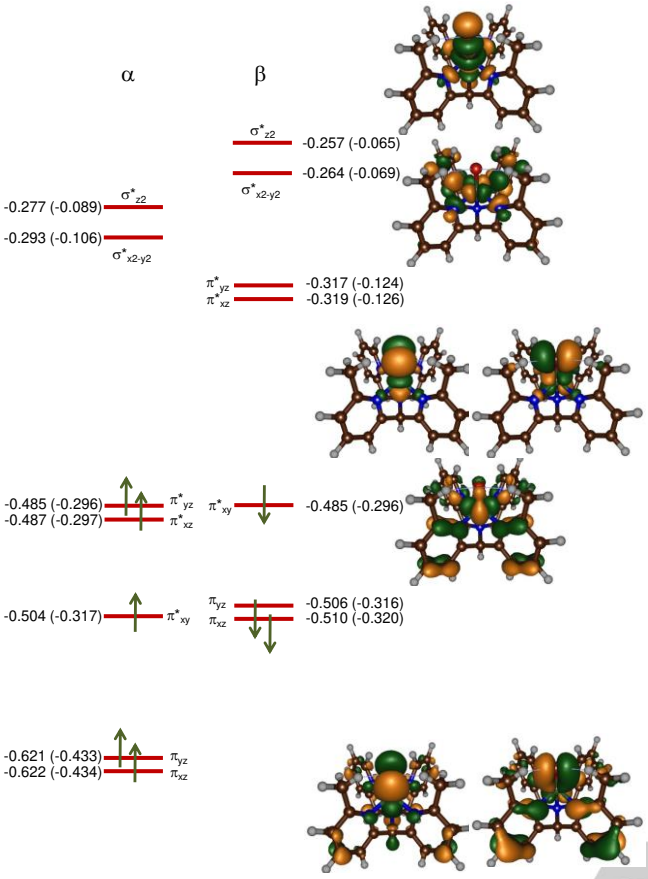

Figure 8. Orbital shapes and energies of ^{3}**2b** as calculated at UB3LYP/BS1 and UB3LYP/BS2 (in parenthesis) in Gaussian. Orbital energies are given in kcal mol^{-1}.

Moreover, when the orbital energies are compared relative to the β-spin π^*_{xy} molecular orbital, we only see minor shifts in energy levels between the two structures. Consequently, the addition of methyl substituents to the N4Py scaffold nearby the oxo group in the iron(IV)-oxo species has little effect on the electronic configuration of the oxidant and the orbital energies and shapes. Thus, any change in reactivity must therefore come from differences in substrate approach through electrostatic interactions. Further evidence for the small changes in orbital energies comes from the calculated (adiabatic) electron affinities of the various complexes, whereby we find values of 119.3, 119.2 and 120.7 kcal mol^{-1} for ^{3}**1b**, ^{3}**2b** and ^{3}**3b**, respectively. Therefore, any change in rate constant should result from second-coordination sphere effects through interactions of the approaching substrate with the oxidant.

Subsequently, we investigated the oxygen atom transfer from ^{3,5}**2b** and ^{3,5}**3b** to *para*-Z-substituted thioanisole with Z = OCH_3, CH_3, H, Cl and NO_2. As before, the reactions are concerted with a single oxygen atom transfer to form sulfoxide products (^{3,5}**P**$_{SO,Z}$) with a transition state ^{3,5}**TS**$_{SO,Z}$. Figure 9 shows the general energy landscape for the reactions starting from ^{3,5}**2b** and ^{3,5}**3b** with *para*-H-thioanisole as an example. Although the triplet spin state is the ground state upon reaching the S–O bond formation transition state, a spin state crossing from the triplet to the quintet spin state occurs and hence ^{5}**TS**$_{SO}$ is well below ^{3}**TS**$_{SO}$. As a matter of fact, ^{5}**TS**$_{SO}$ is only a fraction higher in energy than the quintet spin reactants, which implies the reaction must be really fast on a quintet spin state surface. Energetically, for structure **2b** the quintet spin state sulfoxidation barrier is $\Delta E^{‡}$+ZPE = 5.3 kcal mol^{-1}, while it is much lower for **3b** where we find a value of only 1.5 kcal mol^{-1}. Despite the large drop in barrier height between ^{5}**TS**$_{SO,H}$ for **2b** versus **3b** they are geometrically alike (Figure S17, Supporting Information). The drop in barrier height, therefore, must originate from second-coordination sphere effects rather than first-coordination sphere effects or changes in the oxidant structure. In particular, a change in N_{ax}–Fe–O angle is seen for all transition states. Thus, as discussed above in Figure 7, the ^{3,5}**2b** structures have an almost linear N_{ax}–Fe–O angle of about 177°, whereas in ^{3,5}**3b** the angle is slightly tilted to 172°–174°. In the sulfoxidation transition states displayed in Figure 9 all structures have an N_{ax}–Fe–O angle in the range 168 – 172.5°. Therefore, the change in angle is stronger for complexes ^{3,5}**2b** than for ^{3,5}**3b**, where the metal stays in virtually the same position as in reactants. As a result of smaller changes in geometry the sulfoxidation barriers are considerably lower. The overall sulfoxidation reaction is exothermic by 12.8 (for **2b**) and 17.8 (for **3b**) kcal mol^{-1} to form products.

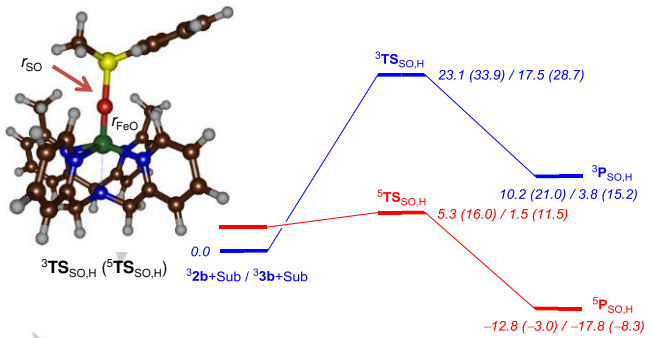

Z	r_{FeO}		r_{SO}		Imag freq	
	triplet	quintet	triplet	quintet	triplet	quintet
H-2b	1.764	1.773	2.072	2.196	i473	i116
H-3b	1.768	1.777	2.078	2.230	i500	i76

Figure 9. Calculated sulfoxidation reaction mechanism for the reaction of ^{3,5}**2b**/^{3,5}**3b** with *p*-H-thioanisole (Sub) obtained at UB3LYP/BS1//UB3LYP/BS2. Energies (free energies) are in kcal mol^{-1} and contain solvent and zero-point corrections. Quintet spin data in parenthesis.

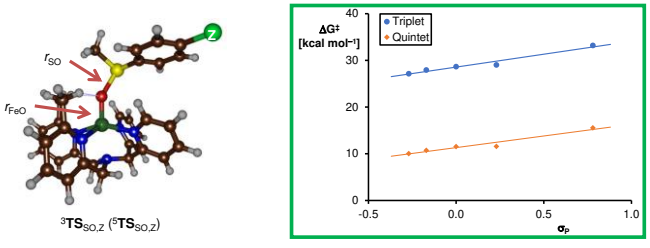

Z	r_{FeO}	r_{SO}	Imag freq
OCH_3	1.765 (1.786)	2.090 (2.218)	i491 (i146)
CH_3	1.765 (1.775)	2.084 (2.241)	i495 (i72)
H	1.768 (1.777)	2.078 (2.230)	i500 (i76)
Cl	1.774 (1.786)	2.070 (2.197)	i507 (i130)
NO_2	1.784 (1.792)	2.052 (2.166)	i519 (i158)

Figure 10. Transition state geometries for the reaction of ^{3,5}**3b** with *para*-Z-thioanisole (Z = OCH_3, CH_3, H, Cl and NO_2) as calculated at UB3LYP/BS1 in

Gaussian. Data represent the Fe–O and S–O bond lengths in angstroms and the imaginary frequency of the transition state in cm^{-1}. Quintet spin data is given in parenthesis.

Optimized geometries of the triplet and quintet spin transition states for the reaction of ^{3,5}**3b** with *para*-Z-thioanisole are given in Figure 10. In the transition state, the Fe–O distance is elongated from 1.654 Å in ^{3}**3b** and 1.647 Å in ^{5}**3b** to values ranging from 1.765 – 1.784 Å in ^{3}**TS**$_{SO,Z}$ and from 1.775 – 1.792 Å in the ^{5}**TS**$_{SO,Z}$ structures. A plot of the triplet spin Fe-O bond lengths against σ_p Hammett parameter gives a linear correlation and as such the structure changes smoothly upon replacement of the *para*-Z group of thioanisole (Supporting Information Figure S15). Similar correlations of the S-O and Fe-N_{ax} distances with Hammett parameter σ_P also give a linear correlation. Therefore, the transition state geometries change smoothly depending on the *para*-Z substituent that causes electron-donating or withdrawing properties on the sulfide group.

The imaginary frequency in the triplet spin state is relatively large, namely ranging from i491 cm^{-1} for *para*-OCH_3-thioanisole to i519 cm^{-1} for *para*-NO_2-thioanisole. Interestingly, in the quintet spin state the imaginary frequencies are much lower, *i.e.* i72 – i158 cm^{-1}. Also the imaginary frequency in the transition state follows the Hammett correlation with Hammett parameter (σ_P), which means that the *para*-Z substituent affects the shape of the potential energy surface and broadens it when more electron-withdrawing substituents are added to the *para*-position of the aromatic ring of the substrate. A similar observation was found for *para*-Z-styrene epoxidation by iron(IV)-oxo porphyrins, where also a linear correlation between Hammett σ_P parameter and imaginary frequency was found.[21] These correlations are found irrespective of the spin state surface.

Finally, we investigated hydrogen atom abstraction from ethylbenzene (EB) by ^{3,5}**2b** and ^{3,5}**3b** and the results are given in Figure 11. As can be seen from Figure 11, the approach of substrate onto the iron(IV)-oxo changes upon substitution of the 6th position with methyl groups and in ^{3,5}**2b** the substrate comes from the left, while it enters from the right in ^{3,5}**3b**. The methyl groups form weak C–H---O hydrogen bonding interactions that stabilize the oxo group and hold it in a specific orientation. Nevertheless, the C–H and O–H distances do not vary dramatically between the structures in the triplet spin state with values of 1.322 (1.303) Å for the C–H interaction and 1.289 (1.316) Å for the O–H distance in ^{3}**TS**$_{HA,2b}$ (^{3}**TS**$_{HA,3b}$), respectively. All triplet spin state transition state structures have a large imaginary frequency for the C--H--O stretch vibration. Values of those magnitudes typically correspond to significant amount of tunneling and a large kinetic isotope effect as also reported experimentally (see above).[22] Despite similar bond lengths the triplet spin HAA barrier for **3b** is 2.0 kcal mol^{-1} lower in energy than that for **2b**, which matches the experimental rate changes well. Lower in energy; however, are the quintet spin hydrogen atom abstraction barriers, which are 7.9 and 4.0 kcal mol^{-1} for system **2b** and **3b**. Therefore, in line with the oxygen atom transfer to sulfides, also the hydrogen atom abstraction transition states are lower for **3b** as compared to **2b**. These rate changes obtained computationally match the experimentally determined trends from Figure 5 and 6 excellently and show that **3b** is a much better oxidant than **2b** for oxidation reactions.

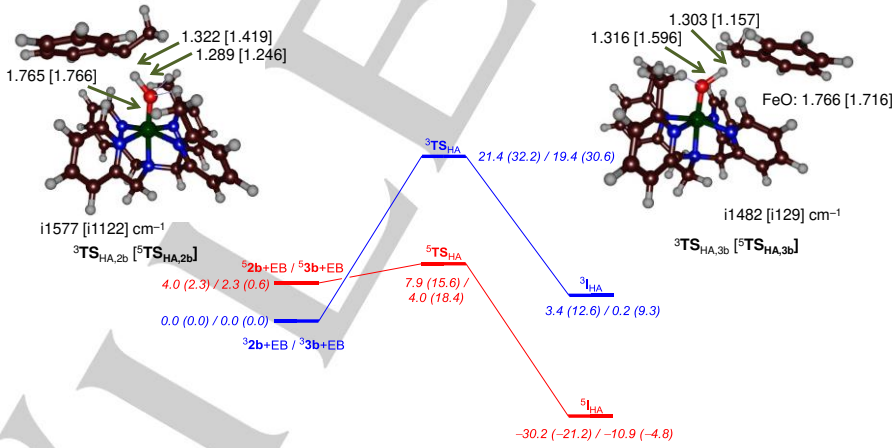

Figure 11. Hydrogen atom abstraction energies for the reaction of ^{3,5}**2b** and ^{3,5}**3b** with ethylbenzene as calculated at UB3LYP/BS1//UB3LYP/BS2 in Gaussian. Energies (in kcal mol^{-1}) represent $\Delta E+ZPE+E_{solv}$ values with free energies (at 298K) in parenthesis. Transition state geometries give bond lengths in angstroms and the imaginary frequency in cm^{-1}.

Discussion

To understand the reactivity differences of **1b**, **2b** and **3b**, we analyzed the thermochemical and electronic properties of the reactant complexes and set up a valence bond model to describe their oxidative differences. The electronic changes for the hydrogen atom abstraction from substrate by the iron(IV)-oxo complexes ^{5}**1b**, ^{5}**2b** and ^{5}**3b** in the quintet spin state is depicted in Scheme 1. As described above in Figure 8 all complexes have an orbital occupation with $\pi_{xz}^2\ \pi_{yz}^2\ \pi^*_{xy}{}^1\ \pi^*_{xz}{}^1\ \pi^*_{yz}{}^1\ \sigma^*_{x2-y2}{}^1$ configuration as identified in Scheme 1 with dots for each electron, while a line separating two dots represents a doubly occupied orbital. Thus, the π_{xz}/π^*_{xz} and π_{yz}/π^*_{yz} pairs of orbitals form two three-electron bonds along the Fe–O axis. In addition, there are two unpaired electrons with dominant contribution on iron in the *xy*-plane, namely π_{xy} and σ^*_{x2-y2}. Finally, the substrate has a doubly occupied σ_{CH} orbital for the C–H bond that is activated in the process.

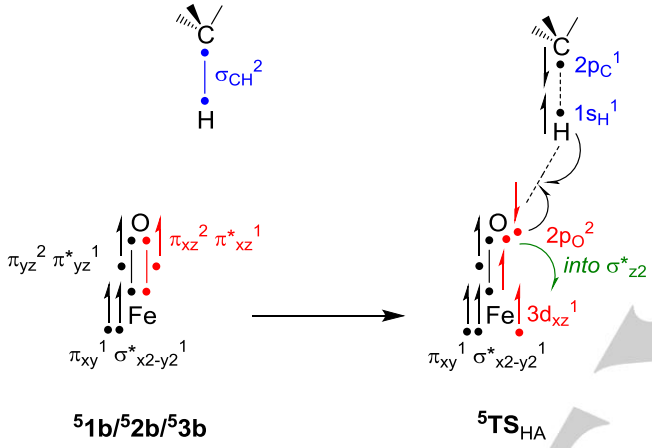

Scheme 1. Valence bond orbital diagram for the electronic changes during hydrogen atom abstraction.

Upon hydrogen atom abstraction, the σ_{CH} bond splits back into atomic orbitals and the leaving H-atoms pairs its electron up with a 2p electron on oxygen. The latter originates from the three-electron π_{xz}/π^*_{xz} pair of orbitals (highlighted in red in Scheme 1) that revert back to atomic orbitals. The other two electrons lead to the nonbonding $3d_{xz}$ with one electron and the σ^*_{z2} orbital with one electron. We previously showed that based on these electron-transfer mechanisms, the hydrogen atom abstraction barrier is correlated with the energy to break the π_{xz}/π^*_{xz} bond, the energy to break the σ_{CH} bond and the energy to form the σ_{OH} orbital for the interaction of $2p_O$ with $1s_H$.[23] As follows from Scheme 1, the oxidation state of iron is reduced from iron(IV) to iron(III) during the hydrogen atom abstraction. Therefore, we decided to do a thermochemical analysis on the physical chemical properties of complexes **1b**, **2b** and **3b** and, particularly, focus on the electron and proton abstraction ability. Thus, the electron affinity (EA) for the one-electron reduction of the triplet spin iron(IV)-oxo complexes were calculated from the adiabatic energy differences (at $\Delta E+ZPE+E_{solv}$) with the iron(III)-oxo complex, see Figure 12. Interestingly, the electron affinity of the three complexes is virtually the same and ranges from 119.2 kcal mol^{-1} for **2b** to 120.7 kcal mol^{-1} for **3b**. Consequently, the changes in reactivity pattern do not originate from differences in the reduction potential of the three complexes.

Subsequently, we calculated the energy for the iron(IV)-oxo species to abstract a hydrogen atom as the energy difference between the iron(III)-hydroxo complex and the sum of the iron(IV)-oxo and a hydrogen atom, which is termed the O–H bond dissociation energy (BDE_{OH}). Similar to the electron affinity (EA) values, the BDE_{OH} values of **1b**, **2b** and **3b** are very close in energy and range from 90.9 kcal mol^{-1} for **2b** to 92.4 kcal mol^{-1} for **3b**. Previously, the BDE_{OH} of the oxidant was correlated with the rate constant for hydrogen atom abstraction and as such would imply similar HAA barriers from substrates.[24] To complement the reaction cycle in Figure 12, we also calculated the acidity of the iron(III)-hydroxo complex (ΔH_{acid}). Obviously, as there are little changes between the complexes for the EA and BDE_{OH} values, also no dramatic changes for the acidity are seen.

Therefore, the three complexes **1b**, **2b** and **3b** have similar physical chemical properties and as a result should also show comparable reactivity patterns with substrates. The fact that this is not the case means external perturbations must be at play and influence the reactivity of these oxidants with substrates. Most likely the reaction rates are affected due to differences in approach of the substrate to the oxidant, which must show structural and electronic differences. To understand the reactivity differences, we did a detailed analysis of the structural and electronic differences of the rate-determining transition states.

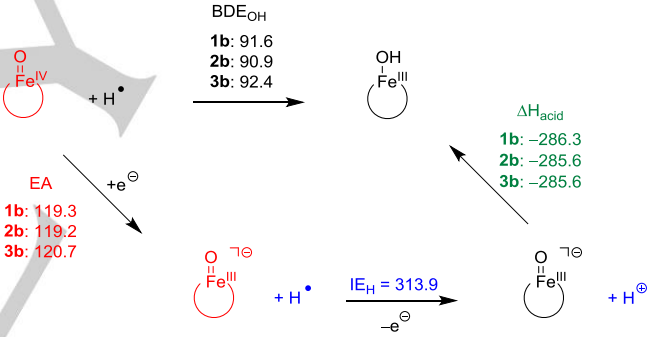

Figure 12. Thermochemical analysis of the differences of structure **1b**, **2b** and **3b** in electron affinity (EA), gas-phase acidity (ΔH_{acid}) and O–H bond strength (BDE_{OH}) with values in kcal mol^{-1}.

In order to identify the structural differences between the rate-determining transition states better, we give an overlay of ^{5}**TS**$_{SO,2b}$ and ^{5}**TS**$_{SO,3b}$, on one hand, and ^{5}**TS**$_{EB,2b}$ and ^{5}**TS**$_{EB,3b}$ on the other hand in Figure 13. As can be seen from Figure 13, the substrate is located in roughly the same position with respect to the oxidant. However, the metal center has shifted slightly within the ligand scaffold. Thus, in ^{5}**TS**$_{SO,3b}$ and ^{5}**TS**$_{EB,3b}$ the metal is located nearby the center of the four pyridine nitrogen atoms that give Fe–N distances within a range of 0.038 and 0.018 Å, respectively. By contrast, for the structures originating from **2b** the Fe–N distances are much wider apart (0.089 and 0.090 Å), so that the metal is not located in the center of the ligand scaffold. The deviation of the metal from the axis will affect the orbital shapes and particularly influence the energy level of the σ^*_{z2} orbital that accepts one electron during the rate-determining step. Interestingly, although the metal is displaced from the center, the group spin densities for ^{5}**TS**$_{SO,2b}$ and ^{5}**TS**$_{SO,3b}$ are virtually the same. Specifically, the complexes give a spin of 3.82/3.84 on iron, 0.27/0.28 on oxygen and –0.43/–0.47 on the substrate.

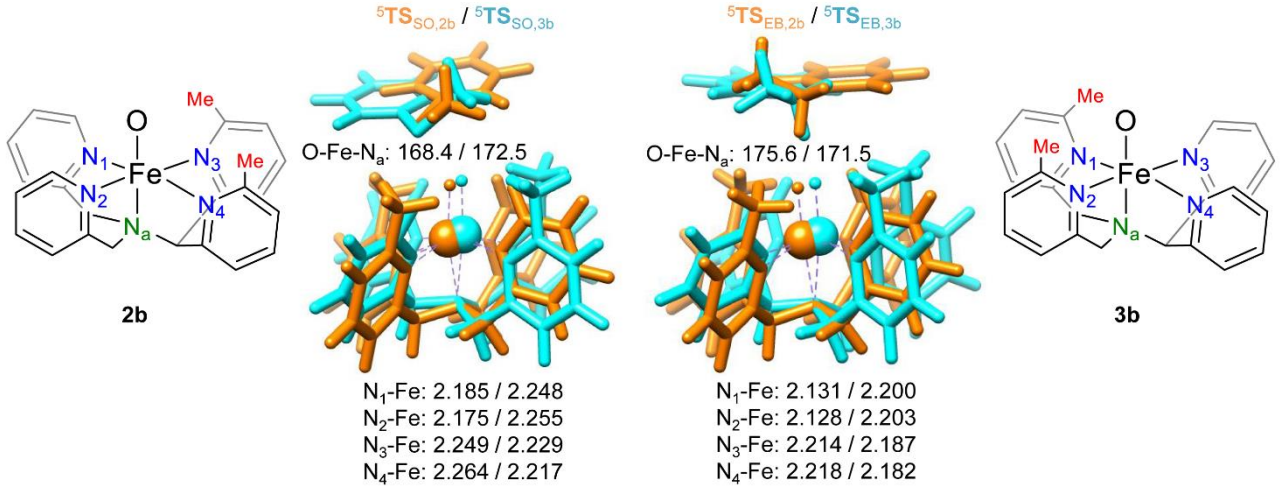

Figure 13. Overlay of optimized geometries of the quintet spin transition states for sulfoxidation and hydrogen atom abstraction by ^{5}**2b** and ^{5}**3b**. Bond lengths are given in angstroms and the O-Fe-N_{ax} angle is in degrees.

These spin densities indeed confirm the electron transfer as proposed in Scheme 1 that leave a down-spin electron on the substrate antiferromagnetically coupled to five unpaired metal-based electrons. Overall, the sulfoxidation barrier heights vary little in electronic configuration despite the large energetic differences. Overall, the calculations show that methyl substituents on the 6-position as in **3b** has an effect on the position of the metal in the ligand framework so that the metal is pulled back into the center of the four pyridine rings during the rate-determining transition state. This has a dramatic effect on lowering the barrier height and consequently the reaction rate due to more favorable overlap between the donating (π^*_{xz}) and accepting (σ^*_{z2}) orbital of the electron even though the reactant complexes do not appear to be systematically different. As such the methyl substituents masquerade the oxidant and effectively position substrate and oxidant for ideal hydrogen atom transfer or oxygen atom transfer reactions.

Conclusions

The reactivity of nonheme ferryl-oxo systems are very difficult to generalize and rational optimization of the ligand scaffolds are very tricky as these systems are extremely sensitive to backbone modifications. However, with the benchmarking of the existing and new iron(IV)-oxo complexes in oxidation reactions, we provided an experimental overview of the various reactivity trends. The theoretical study allows us to understand the fine interplay between electronic and steric effects generated by substituents that can be utilized as guidelines for a more rational synthetic approach to develop more efficient and selective systems. Overall, this research highlights the intricate details of subtle modifications to the primary- and secondary-coordination sphere of mononuclear nonheme iron(IV)-oxo model systems in an octahedral environment that brings forth the competitiveness of electronic and steric factors that influence their reactivity. With the synthesis and characterization of two new pentadentate ligand frameworks, that are isomeric in mass and geometry, we have evidenced that the corresponding iron(IV)-oxo complexes inhabit differences in reactivity profiles towards HAA and OAT reactions. In fact, this study is unique of its kind where regioselective substitution by methyl moieties in the same ligand skeleton provoke substantially different reactivity of the oxo species. Not only that, the methyl groups shield the bulkier substrates like 9,10-DHA, fluorine and mainly triphenylmethane to make the catalysts reluctant towards these substrates, a phenomenon not observed before. Computational modelling rules out the electronic features of the complexes under study and establishes that a steric factor is the driving force behind this eccentric reactivity. Indeed, the methyl groups employed at the specified positions act as shafts to position the substrate and oxidant in a definite orientation in space. These substituents direct the corridors of substrate=approach to the active site thereby tuning the efficiency of hydrogen or oxygen atom transfer reaction similar to what enzymatic catalysts do in proteins that channel the substrate and position the oxidant in an ideal conformation.

Experimental Section

Materials and Methods

All chemicals were obtained from Sigma Aldrich Chemical Co., and were of the best available purity and used without further purification unless otherwise stated. Solvents were dried according to published procedures [25] and distilled under argon prior to use. $H_2{}^{18}O$ (99.9% pure and enrichment 97.1 atom%) was purchased from Berry and Associates (Icon Isotopes). Substrates were passed through silica before reactivity study. Ethyl chloroformate, 95%, was purchased from Avra synthesis Pvt. Ltd. and purified prior to use. Metal complexes, including $[Fe^{II}(N4Py)](ClO_4)_2$ (**1a**), $[Fe^{II}(^{Me}N4Py)](ClO_4)_2$ (**2a**) and $[Fe^{II}(N4Py^{Me})](ClO_4)_2$ (**3a**) were synthesized inside a Jacomex glovebox filled with argon using procedures as described in the Supporting Information. Subsequently, the iron(IV)-oxo complexes, *i.e.* $[Fe^{IV}(O)(N4Py)]^{2+}$ (**1b**), $[Fe^{IV}(O)(^{Me}N4Py)]^{2+}$ (**2b**) and $[Fe^{IV}(O)(N4Py^{Me})]^{2+}$ (**3b**) were prepared

from their corresponding iron(II) complexes with 1.5 equivalents of $PhI(OAc)_2$ in CH_3CN at ambient temperature and pressure.

Characterization

UV-vis spectra were recorded on a Hewlett Packard 8453 spectrophotometer equipped with either constant temperature circulating water bath or a liquid nitrogen cryostat (Unisoku) with a temperature controller. High Resolution electrospray ionization-mass spectra (ESI-MS) were recorded on a Waters (Micromass MS Technologies) Q-TOF Premier mass spectrometer by infusing samples directly into the source at 15 μL min^{-1} using a syringe pump. The spray voltage was set at 2 kV and the capillary temperature at 80°C unless otherwise mentioned. Nuclear Magnetic Resonance (NMR) spectra were recorded on Bruker Avance III HD 600 MHz spectrometer and Jeol Advanced Solution State 400 MHz spectrometer (JNM-ECZ400S) using TMS as internal standard under ambient conditions. Product analysis of the reaction mixtures were done by ESI-MS, NMR (^1H and ^{13}C) with a Varian 400/100 MHz spectrometer and LCMS with WATERS ACQUITY UPLC equipped with a variable wavelength UV-200 detector. The crystal structure was recorded on an Agilent Single Crystal X-Ray Diffractometer (XRD) equipped with Mo X-ray source (Mova), CCD detector (Eos), Oxford cryo system and crystal AlisPRO and Autochem software.

Kinetics experiments

Upon addition of substrate to *in situ* generated iron(IV)-oxo species, the decay of the absorption band against time was monitored in the UV-vis spectrum. Substrate concentrations were maintained in excess to obtain pseudo first-order reaction conditions. Kinetic profiles were obtained at four different substrate concentrations which were plotted against the k_{obs} values to obtain a linear correlation and enabled us to determine second-order rate constants (k_2) for each reaction. The slopes pass through the origin to ensure minimum standard deviation and zero intercept on either axes. All UV-vis spectra were measured in a 10 mm quartz cell.

Computation

Density functional theory calculations were performed for the reaction mechanisms of **1b**, **2b** and **3b** with ethylbenzene and *para*-Z-thioanisole with Z = OCH_3, CH_3, H, Cl and NO_2. Extensive benchmarking and testing of computational methods and procedures on this particular system was reported in previous work on the reactivity of $[Fe^{IV}(O)(N4Py)]^{2+}$ with *para*-Z-substituted thioanisole as well as dimethylsulfide.[26] These studies showed that the methods used here give excellent agreement with experimentally determined free energies and enthalpies of activation. In particular, experimental rate constants were converted into free energy of activation values using transition state theory. Those values were within 4 kcal mol^{-1} from those calculated with DFT methods as used in this work. Full geometry optimizations (without constraints) were done with either UB3LYP/BS1 or UB3LYP/BS2 level of theory in Gaussian-09.[27–29] BS1 stands for LACVP with core potential on iron and 6-31G on the rest of the atoms, while BS2 represents a triple-ξ basis set (LACV3P+ on iron and 6-311+G* on the rest of the atoms). The calculations included a conductor polarized continuum model (CPCM) with a dielectric constant mimicking acetonitrile. In general, calculations obtained with UB3LYP/BS2 and UB3LYP/BS1//UB3LYP/BS2 gave virtually the same structures and energies. Transition states were characterized with a frequency calculation that gave a single imaginary frequency for the correct mode. In addition, for a selection of structures intrinsic reaction coordinate (IRC) scans were performed. These IRCs connected the transition states to the reactants in one direction and to products in the reverse direction.

Acknowledgements

Research support was provided by the Department of Science and Technology (SERB), India (EMR/2014/000279) to CVS. SdV and CVS thank the British Council for a UK-India Education and Research Initiative grant (DST/INT/UK/P-151/2017). DK acknowledges financial support from the Department of Biotechnology, New Delhi (BT/PR14510/BID/07/334/2010). We also thank Central Instrumentation Facility (CIF) IIT Guwahati for providing instrumental facilities.

Conflicts of interest

There are no conflicts to declare.

Keywords: • Iron-oxo • kinetics • DFT analysis • biomimetic models • Steric effect • inorganic reaction mechanism.

[1] a) M. Costas, M. P. Mehn, M. P. Jensen, L. Que Jr., *Chem. Rev*. **2004**, *104*, 939-986; b) M. M. Abu-Omar, A. Loaiza, N. Hontzeas, *Chem. Rev.* **2005**, *105*, 2227-2252; c) C. Krebs, D. G. Fujimori, C. T. Walsh, J. M. Bollinger Jr., *Acc. Chem. Res*. **2007**, *40*, 484-492; d) P. C. A. Bruijnincx, G. van Koten, R. J. M. Klein Gebbink, *Chem. Soc. Rev*. **2008**, *37*, 2716-2744; e) E. I. Solomon, K. M. Light, L. V. Liu, M. Srnec, S. D. Wong, *Acc. Chem. Res*. **2013**, *46*, 2725-2739; f) K. Ray, F. F. Pfaff, B. Wang, W. Nam, *J. Am. Chem. Soc*. **2014**, *136*, 13942-13958; g) X. Engelmann, I. Monte-Pérez, K. Ray, *Angew. Chem. Int. Ed*. **2016**, *55*, 7632-7649.

[2] a) B. Meunier, S. P. de Visser, S. Shaik, *Chem. Rev*. **2004**, *104*, 3947-3980; b) I. G. Denisov, T. M. Makris, S. G. Sligar, I. Schlichting, *Chem. Rev*. **2005**, *105*, 2253-2278; c) P. R. Ortiz de Montellano, *Chem. Rev*. **2010**, *110*, 932-948; d) D. Li, Y. Wang, K. Han, *Coord. Chem. Rev*. **2012**, *256*, 1137-1150; e) M. R. A. Blomberg, T. Borowski, F. Himo, R.-Z. Liao, P. E. M. Siegbahn, *Chem. Rev*. **2014**, *114*, 3601-3658; f) S. P. de Visser, D. Kumar, (Eds., *Iron-containing enzymes: Versatile catalysts of hydroxylation reaction in nature*), RSC Publishing, Cambridge (UK), **2011**.

[3] a) E. I. Solomon, T. C. Brunold, M. I. Davis, J. N. Kemsley, S. K. Lee, N. Lehnert, F. Neese, A. J. Skulan, Y. S. Yang, J. Zhou, *Chem. Rev*. **2000**, *100*, 235-349; b) J. U. Rohde, J. H. In, M. H. Lim, W. W. Brennessel, M. R. Bukowski, A. Stubna, E. Münck, W. Nam, L. Que Jr, *Science*, **2003**, *299*, 1037-1039; c) C. V. Sastri, J. Lee, K. Oh, Y. J. Lee, T. A. Jackson, K. Ray, H. Hirao, W. Shin, J. A. Halfen, J. Kim, L. Que Jr, S. Shaik, W. Nam, *Proc. Natl. Acad. Sci. USA*, **2007**, *104*, 19181-19186; d) P. Comba, S. Wunderlich, *Chem. Eur. J*. **2010**, *16*, 7293-7299; e) S. V. Kryatov, E. V. Rybak-Akimova, S. Schindler, *Chem. Rev*. **2005**, *105*, 2175-2226.

[4] a) M. Lubben, A. Meetsma, E. C. Wilkinson, B. Feringa, L. Que Jr., *Angew. Chem. Int. Ed*. **1995**, *34*, 1512-1515; b) J. Kaizer, E. J. Klinker, N. Y. Oh, J.-U. Rohde, W. J. Song, A. Stubna, J. Kim, E. Münck, W. Nam, L. Que Jr., *J. Am. Chem. Soc*. **2004**, *126*, 472-473; c) E. J. Klinker, T. A. Jackson, M. P. Jensen, A. Stubna, G. Juhász, E. L. Bominaar, E. Münck, L. Que Jr., *Angew. Chem. Int. Ed*. **2006**, *45*, 7394-7397; d) D. Wang, K. Ray, M. J. Collins, E. R. Farquhar, J. R. Frisch, L. Gómez, T. A. Jackson, M. Kerscher, A. Waleska, P. Comba, M. Costas, L. Que Jr., *Chem. Sci*. **2013**, *4*, 282-292.

[5] a) A. C. McQuilken, Y. Jiang, M. A. Siegler, D. P. Goldberg, *J. Am. Chem. Soc*. **2012**, *134*, 8758-8761; b) S. Sahu, L. R. Widger, M. G. Quesne, S. P. de Visser, H. Matsumura, P. Moënne-Loccoz, M. A. Siegler, D. P. Goldberg, L. R. Widger, C. G. Davies, T. Yang, M. A. Siegler, O. Troeppner, G. N. L. Jameson, I. Ivanović-Burmazović, D. P. Goldberg, *J. Am. Chem. Soc*. **2013**, *135*, 10590-10593; c) L. R. Widger, C. G. Davies, T. Yang, M. A. Siegler, O. Troeppner, G. N. L. Jameson, I. Ivanović-Burmazović, D. P. Goldberg, *J. Am. Chem. Soc*. **2014**, *136*, 2699-2702; d) S. Sahu, M. G. Quesne, C. G. Davies, M. Dürr, I. Ivanović-Burmazović, M. A. Siegler, G. N. L. Jameson, S. P. de Visser, D. P. Goldberg, *J. Am. Chem. Soc*. **2014**, *136*, 13542-13545; e) S. Sahu, B. Zhang, C. J. Pollock, M. Dürr, C. G. Davies, A. M. Confer, I. Ivanović-Burmazović, M. A. Siegler, G. N. L. Jameson, C. Krebs, D. P. Goldberg, *J. Am. Chem. Soc*. **2016**, *138*, 12791-12802; f) M. Mitra, H. Nimir, S. Demeshko, S. S. Bhat, S. O. Malinkin, M. Haukka, J. Lloret-Fillol, G. C. Lisensky, F. Meyer, A. A. Shteinman, W. R. Browne, D. A.

Hrovat, M. G. Richmond, M. Costas, E. Nordlander, *Inorg. Chem.* **2015**, *54*, 7152-7164; g) S. Rana, A. Dey, D. Maiti, *Chem. Commun.* **2015**, *51*, 14469-14472.

[6] a) W. Rasheed, A. Draksharapu, S. Banerjee, V. G. Young Jr, R. Fan, Y. Guo, M. Ozerov, J. Nehrkorn, J. Krzystek, J. Telse, L. Que Jr, *Angew. Chem. Int. Ed.* **2018**, *57*, 9387-9391; b) G. Mukherjee, C. W. Z. Lee, S. S. Nag, A. Alili, F. G. Cantú Reinhard, D. Kumar, C. V. Sastri, S. P. de Visser, *Dalton Trans.* **2018**, *47*, 14945-14957; c) S. Rana, J. P. Biswas, A. Sen, M. Clémancey, G. Blondin, J.-M. Latour, G. Rajaraman, D. Maiti, *Chem. Sci.* **2018**, *9*, 7843-7858.

[7] Y. Zang, J. Kim, Y. Dong, E. C. Wilkinson, E. H. Appelman, L. Que Jr., *J. Am. Chem. Soc.* **1997**, *119*, 4197-4205.

[8] A. N. Biswas, M. Puri, K. K. Meier, W. N. Oloo, G. T. Rohde, E. L. Bominaar, E. Münck, L. Que Jr., *J. Am. Chem. Soc.* **2015**, *137*, 2428-2431.

[9] M. S. Seo, N. H. Kim, K.-B. Cho, J. E. So, S. K. Park, M. Clémancey, R. G. Serres, J.-M. Latour, S. Shaik, W. Nam, *Chem. Sci.* **2011**, *2*, 1039-1045.

[10] a) C. E. Macbeth, A. P. Golombek, V. G. Young Jr, C. Yang, K. Kuczera, M. P. Hendrich, A. S. Borovik, *Science,* **2000**, *289*, 938-941; b) J. England, M. Martinho, E. R. Farquhar, J. R. Frisch, E. L. Bominaar, E. Münck, L. Que Jr, *Angew. Chem. Int. Ed.* **2009**, *48*, 3622-3626; c) J. P. Bigi, W. H. Harman, B. Lassalle-Kaiser, D. M. Robles, T. A. Stich, J. Yano, R. D. Britt, C. J. Chang, *J. Am. Chem. Soc.* **2012**, *134*, 1536-1542.

[11] a) A. K. Patra, M. M. Olmstead, P.K. Mascharak, *Inorg. Chem.* **2002**, *41*, 5403-5409; b) S. Kundu, J. V. K. Thompson, A. D. Ryabov, T. J. Collins, *J. Am. Chem. Soc.* **2011**, *133*, 18546-18549; c) S. A. Wilson, J. Chen, S. Hong, Y.-M. Lee, M. Clémancey, R. Garcia-Serres, T. Nomura, T. Ogura, J.-M. Latour, B. Hedman, K. O. Hodgson, W. Nam, E. I. Solomon, *J. Am. Chem. Soc.* **2012**, *134*, 11791-11806; d) I. Prat, A. Company, T. Corona, T. Parella, X. Ribas, M. Costas, *Inorg. Chem.* **2013**, *52*, 9229-9244; e) E. Wong, J. Jeck, M. Grau, A. J. P. White, G. J. P. Britovsek, *Catal. Sci. Technol.* **2013**, *3*, 1116-1122; f) M. Mitra, J. Lloret-Fillol, M. Haukka, M. Costas, E. Nordlander, *Chem. Commun*, **2014**, *50*, 1408-1410; g) X. Sun, C. Geng, R. Huo, U. Ryde, Y. Bu, J. Li, *J. Phys. Chem. B.* **2014**, *118*, 1493-1500; h) R. Turcas, D. Lakk-Bogath, G. Speier, J. Kaizer, *Dalton. Trans.* **2018**, *47*, 3248-3252.

[12] Single crystals of **2a** were obtained by using Fe(II)-tetrafluoroborate salt instead of Fe(II)-perchlorate.

[13] a) G. Roelfes, M. Lubben, K. Chen, R. Y. N. Ho, A. Meetsma, S. Genseberger, R. M. Hermant, R. Hage, S. K. Mandal, V. G. Young Jr., Y. Zang, H. Kooijman, A. L. Spek, L. Que Jr., B. L. Feringa, *Inorg. Chem.* **1999**, *38*, 1929-1936; b) A. L. Spek, M. F. J. Schoondergang, B. L. Feringa, CCDC 232796, *CSD Communication*, **2004**.

[14] M. S. Seo, J.-H. In, S. O. Kim, N. Y. Oh, J. Hong, J. Kim, L. Que Jr., W. Nam, *Angew. Chem. Int. Ed.* **2004**, *43*, 2417-2420.

[15] a) E. J. Klinker, J. Kaizer, W. W. Brennessel, N. L. Woodrum, C. J. Cramer, L. Que Jr., *Angew. Chem. Int. Ed.* **2005**, *44*, 3690-3694; b) K. Ray, J. England, A. T. Fiedler, M. Martinho, E. Münck, L. Que Jr., *Angew. Chem. Int. Ed.* **2008**, *47*, 8068-8071; c) A. Company, G. Sabenya, M. González-Béjar, L. Gómez, M. Clémancey, G. Blondin, A. J. Jasniewski, M. Puri, W. S. Browne, J. M. Latour, L. Que Jr., M. Costas, J. PérezPrieto, J. Lloret-Fillol, *J. Am. Chem. Soc.* **2014**, *136*, 4624-4633.

[16] a) M. H. Lim, J.-U. Rohde, A. Stubna, M. R. Bukowski, M. Costas, R. Y. N. Ho, E. Münck, W. Nam, L. Que Jr., *Proc. Natl. Acad. Sci. U.S.A.* **2003**, *100*, 3665-3670; b) M. S. Seo, H. G. Jang, J. Kim, W. Nam, *Bull. Korean. Chem. Soc.* **2005**, *26*, 971-974; c) M. You, M. S. Seo, K. M. Kim, W. Nam, J. Kim, *Bull. Korean. Chem. Soc.* **2006**, *27*, 1140-1144; d) W. Nam, *Acc. Chem. Res.* **2007**, *40*, 522-531; e) S. Paria, S. Chatterjee, T. K. Paine, *Inorg. Chem.* **2014**, *53*, 2810-2821; f) D. Sheet, T. K. Paine, *Chem. Sci.* **2016**, **7**, 5322-5331.

[17] a) A. K. Vardhaman, P. Barman, S. Kumar, C. V. Sastri, D. Kumar, S. P. de Visser, *Angew. Chem. Int. Ed.* **2013**, *52*, 12288-12292; b) S. Kumar, A. S. Faponle, P. Barman, A. K. Vardhaman, C. V. Sastri, D. Kumar, S. P. de Visser, *J. Am. Chem. Soc.* **2014**, *136*, 17102-17115.

[18] A. K. Vardhaman, S. Sikdar, C. V. Sastri, *Ind. J. Chem.* **2011**, *50A*, 427-431.

[19] a) D. Kumar, H. Hirao, L. Que Jr., S. Shaik, *J. Am. Chem. Soc.* **2005**, *127*, 8026-8027; b) S. P. de Visser, *J. Am. Chem. Soc.* **2006**, *128*, 9813-9824; c) L. Bernasconi, E.-J. Baerends, *Eur. J. Inorg. Chem.* **2008**, 1672-1681; d) S. D. Wong, C. B. Bell III, L. V. Liu, Y. Kwak, J. England, E. E. Alp, J. Zhao, L. Que Jr., E. I. Solomon, *Angew. Chem. Int. Ed.* **2011**, *50*, 3215-3218; e) S. F. Ye, F. Neese, *Proc. Natl. Acad. Sci. USA,* **2011**, *108*, 1228-1233; f) R. Latifi, M. A. Sainna, E. V. Rybak-Akimova, S. P. de Visser, *Chem. Eur. J.* **2013**, *19*, 4058-4068; g) T. Z. H. Gani, H. J. Kulik, *ACS Catal.* **2018**, *8*, 975-986.

[20] a) M. Martinho, F. Banse, J.-F. Bartoli, T. A. Mattioli, P. Battioni, O. Horner, S. Bourcier, J.-J. Girerd, *Inorg. Chem.* **2005**, *44*, 9592-9596; b) A. S. Borovik, *Acc. Chem. Res.* **2005**, *38*, 54-61; c) S. P. de Visser, J.-U. Rohde, J.-M. Lee, J. Cho, W. Nam, *Coord. Chem. Rev.* **2013**, *257*, 381-393; d) N. Y. Lee, D. Mandal, S. H. Bae, M. S. Seo, Y.-M. Lee, S. Shaik, K.-B. Cho, W. Nam, *Chem. Sci.* **2017**, *8*, 5460-5467.

[21] D. Kumar, R. Latifi, S. Kumar, E. V. Rybak-Akimova, M. A. Sainna, S. P. de Visser, *Inorg. Chem.* **2013**, *52*, 7968-7979.

[22] a) S. P. de Visser, *Chem. Eur. J.* **2006**, *12*, 8168–8177; b) L. Ji, A. S. Faponle, M. G. Quesne, M. A. Sainna, J. Zhang, A. Franke, D. Kumar, R. van Eldik, W. Liu, S. P. de Visser, *Chem. Eur. J.* **2015**, *21*, 9083–9092; c) M. G. Quesne, D. Senthilnathan, D. Singh, D. Kumar, P. Maldivi, A. B. Sorokin, S. P. de Visser, *ACS Catal.* **2016**, *6*, 2230–224.

[23] a) S. P. de Visser, *J. Am. Chem. Soc.* **2010**, *132*, 1087-1097; b) X.-X. Li, V. Postils, W. Sun, A. S. Faponle, M. Solà, Y. Wang, W. Nam, S. P. de Visser, *Chem. Eur. J.* **2017**, *23*, 6406-6418; c) A. Timmins, M. G. Quesne, T. Borowski, S. P. de Visser, *ACS Catal.* **2018**, *8*, 8685-8698.

[24] a) L. E. Friedrich, *J. Org. Chem.* **1983**, *48*, 3851-3852; b) J. M. Mayer, *Acc. Chem. Res.* **1998**, *31*, 441-450; c) S. P. de Visser, D. Kumar, S. Cohen, R. Shacham, S. Shaik, *J. Am. Chem. Soc.* **2004**, *126*, 8362-8363.

[25] D. D. Perrin, (Ed.) *Purification of Laboratory Chemicals*. Pergamon Press, Oxford, **1997**.

[26] a) T. Yang, M. G. Quesne, H. M. Neu, F. G. Cantú Reinhard, D. P. Goldberg, S. P. de Visser, *J. Am. Chem. Soc.* **2016**, *138*, 12375-12386; b) F. G. Cantú Reinhard, A. S. Faponle, S. P. de Visser, *J. Phys. Chem. A*, **2016**, *120*, 9805-9814.

[27] a) C. Lee, W. Yang, R. G. Parr, *Phys. Rev. B* **1988**, *37*, 785-789; b) A. D. Becke, *J. Chem. Phys.* **1993**, *98*, 5648-5652.

[28] P. J. Hay and W. R. Wadt, *J. Chem. Phys.* **1985**, *82*, 270-283.

[29] Gaussian 09, Revision D.01, M. J. Frisch, G. W. Trucks, H. B. Schlegel, G. E. Scuseria, M. A. Robb, J. R. Cheeseman, G. Scalmani, V. Barone, B. Mennucci, G. A. Petersson, H. Nakatsuji, M. Caricato, X. Li, H. P. Hratchian, A. F. Izmaylov, J. Bloino, G. Zheng, J. L. Sonnenberg, M. Hada, M. Ehara, K. Toyota, R. Fukuda, J. Hasegawa, M. Ishida, T. Nakajima, Y. Honda, O. Kitao, H. Nakai, T. Vreven, J. A. Montgomery Jr., J. E. Peralta, F. Ogliaro, M. Bearpark, J. J. Heyd, E. Brothers, K. N. Kudin, V. N. Staroverov, R. Kobayashi, J. Normand, K. Raghavachari, A. Rendell, J. C. Burant, S. S. Iyengar, J. Tomasi, M. Cossi, N. Rega, J. M. Millam, M. Klene, J. E. Knox, J. B. Cross, V. Bakken, C. Adamo, J. Jaramillo, R. Gomperts, R. E. Stratmann, O. Yazyev, A. J. Austin, R. Cammi, C. Pomelli, J. W. Ochterski, R. L. Martin, K. Morokuma, V. G. Zakrzewski, G. A. Voth, P. Salvador, J. J. Dannenberg, S. Dapprich, A. D. Daniels, Ö. Farkas, J. B. Foresman, J. V. Ortiz, J. Cioslowski, D. J. Fox, Gaussian, Inc., C. T. Wallingford, **2009**.

Entry for the Table of Contents

FULL PAPER

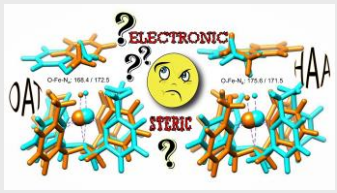

A combined spectroscopy and computational study on engineered iron(IV)-oxo complexes identifies a second-coordination sphere effect that enables better positioning of the iron(IV)-oxo and higher reactivity.

Gourab Mukherjee, Aligulu Alili, Prasenjit Barman, Devesh Kumar, Chivukula V. Sastri and Sam. P. de Visser**

Page No. – Page No.

Interplay between steric and electronic effects: A joint spectroscopy and computational study of nonheme iron(IV)-oxo complexes